

# Topological Polarization Beam Splitter in Dual-Polarization All-Dielectric Valley Photonic Crystals

Xin-Tao He<sup>✉</sup>, Chao-Heng Guo, Guo-Jing Tang<sup>✉</sup>, Meng-Yu Li, Xiao-Dong Chen<sup>✉,\*</sup>, and Jian-Wen Dong<sup>✉,†</sup>

*School of Physics and State Key Laboratory of Optoelectronic Materials and Technologies, Sun Yat-sen University, Guangzhou 510275, China*



(Received 23 August 2022; accepted 3 October 2022; published 31 October 2022)

The recent realization of all-dielectric valley photonic crystals (VPCs) in nanoscale not only provides a standard platform to explore many topological phases of light with protected edge modes, but also shows promising applications for designing high-performance nanophotonic devices. However, the widely reported all-dielectric VPCs are limited to one single polarization, and it is challenging to manipulate the polarization degree of freedom of light and design polarizing devices using VPCs. Here, we design a dual-polarization all-dielectric VPC and propose a topological polarization beam splitter. The phase vortex distributions of bulk modes at different valleys characterize the nonzero valley Chern numbers for both TE and TM polarizations, indicating the implementation of topologically nontrivial dual-polarization band gaps. This leads to dual-polarization valley-dependent edge modes located at interfaces with different shapes. The topological valley transport around sharp-bends is also demonstrated for both TE and TM polarizations. Finally, a harpoon-shaped polarization beam splitter is proposed, and the simulated results confirm the good functionality of polarization separation. Our work shows the flexible control of light in topological photonic systems with the polarization degree of freedom, and has promising applications in polarization multiplexing photonic devices owing to the enlarged the optical information-processing capacity.

DOI: [10.1103/PhysRevApplied.18.044080](https://doi.org/10.1103/PhysRevApplied.18.044080)

## I. INTRODUCTION

The introduction of topology in photonic systems has attracted much attention for the exploration of topological phases of light [1–3]. Recently, based on the robustness of topological states, topological photonics has provided a new paradigm for promising applications in nanophotonic devices. To be compatible with nanofabrication techniques, it is common to apply all-dielectric designs for topological photonic structures, such as dielectric photonic crystals (PCs), coupled resonator optical waveguides, and waveguide arrays [4–19]. With the features of modes operating below the light cone, near quarter-wavelength periodicity, and CMOS-compatible design, the all-dielectric valley photonic crystal (VPC) is one of the representative structures that can demonstrate topological physics and realize high-performance nanophotonic devices [5,6,8,9,20,21]. In principle, to obtain a VPC whose band gap is characterized by the nonzero valley Chern number, one

can break the spatial inversion or mirror symmetry of triangular or honeycomb PCs. Under the suppression of inter-valley scattering between the edge modes of VPCs, topological valley transport has been extensively demonstrated with the realization of photonic waveguides, splitters, and ring resonators [22–25]. Note that all-dielectric VPCs are usually realized in ideal or effective two-dimensional (2D) electromagnetic systems where light propagates within the  $x$ - $y$  plane. Eigenmodes of 2D photonic systems can be classified into two decoupled modes (or polarizations), i.e., the transverse-electric (TE) modes with in-plane electric fields, and the transverse-magnetic (TM) modes with out-of-plane electric fields [26]. Recently, two different schemes for dual-polarization VPCs have been proposed by using a perfect electric conductor or germanium, but they bring absorption loss at telecommunication wavelengths [27,28]. For the more general case, the widely reported all-dielectric VPCs based on silicon are limited to one single (TE or TM) polarization.

Polarization is one of the degrees of freedom (DOF) for molding the flow of light and designing nanophotonic devices. For example, by separately processing the TE- and TM-polarized waves, a polarization beam splitter (PBS) can be designed (generally in a  $1 \times 2$  or  $2 \times 2$

\*chenxd67@mail.sysu.edu.cn

†dongwen@mail.sysu.edu.cn

multiport structure) and this is an important nanophotonic device [29–32]. One can multiplex the polarization DOF to enlarge optical information-processing capacity. It would be interesting if the topological properties of VPCs could be used to design a PBS, which would be promising for the realization of nanophotonic devices with topological robustness and compact size. However, there is a lack of a practical design for a general multiport PBS using VPCs. In this work, we present the dual-polarization all-dielectric VPCs whose unit cell consists of an equilateral triangular air hole in the dielectric background. Two band gaps with different polarizations are obtained and characterized by the same valley Chern numbers, because the direction of the phase vortex of TE bulk modes at the  $K$  or  $K'$  valley is the same as that of TM bulk modes. Valley-dependent edge modes located at interfaces with different shapes, as well as topological valley transport around sharp bends, are numerically demonstrated for both TE and TM polarizations. In addition, we propose a harpoon-shaped PBS based on the dual-polarization feature of the designed VPCs. The simulated transmittances of this PBS confirm the good functionality of TE- and TM-polarized waves splitting within the whole dual-polarization band gap.

## II. DUAL-POLARIZATION ALL-DIELECTRIC VALLEY PHOTONIC CRYSTAL

In an all-dielectric PC, the electromagnetic-duality symmetry is broken, i.e., the ratio of the permittivity to the permeability is not constant over the whole real space. With the broken electromagnetic-duality symmetry, the band structures of the TE and TM polarizations are different as the PC responds differently to the in-plane and out-of-plane electric fields [26]. For example, when considering a honeycomb lattice of a hole-type PC (i.e., air holes located at the corners of the hexagonal unit cell in the dielectric background), the first and second TE bands will be degenerate at the  $K$  point and form a gapless Dirac cone, while the TM Dirac cone is formed by the second and third TM bands [8,9,33]. The difference of Dirac frequencies limits the realization of the complete band gap for both polarizations. On the other hand, one can find a TM Dirac cone between the first and second bands in a honeycomb lattice of a rod-type PC (i.e., dielectric rods at the corners of the hexagonal unit cell) [6,34], but the configuration of the unit cell is quite different to that of the previously mentioned honeycomb lattice of the hole-type PC. In this work, one of the targets is to use the same design of the geometry profile of the PC to achieve dual-polarization Dirac cones in the same frequency range.

For the TE polarization, we start with a hole-type honeycomb PC [Fig. 1(a)]. The unit cell (pink hexagon) consists of two triangular air holes (shaded in white) embedded in the dielectric background (shaded in black). The lattice constant is  $a = 440$  nm, and the side lengths of

air holes are  $s_{1-\text{hc}}$  and  $s_{2-\text{hc}}$ . The dielectric background has a relative permittivity tensor  $\boldsymbol{\epsilon}_r = \text{diag}(n_{\text{TE}}^2, n_{\text{TE}}^2, n_{\text{TM}}^2)$ . Here,  $n_{\text{TE}} = 2.92$  and  $n_{\text{TM}} = 2.51$  are the effective refractive indices, which are based on the refractive indices of the  $\text{TE}_0$  and  $\text{TM}_0$  mode of a 320-nm-thick silicon slab around the wavelength of 1550 nm, respectively [35]. In the calculation of photonic band structures, we perform the plane-wave expansion method by using the eigen-mode solver of the MIT Photonic Bands package [36]. The left panel of Fig. 1(a) shows the first and second TE bulk band structures (i.e.,  $\text{TE}1$  and  $\text{TE}2$ ) of the PC with  $s_{1-\text{hc}} = s_{2-\text{hc}} = 263$  nm (i.e., air-hole filling factor of 0.36), and the frequency degeneracy is achieved at the  $K$  point. The existence of the gapless Dirac cone around the zone corner is protected under the  $C_{3v}$  point group symmetry at the  $K$  point. To obtain the photonic band gap, one can split the degenerate point of the Dirac cone by breaking the inversion symmetry of PCs, which is easy to realize in the honeycomb PC with two inequivalent air holes ( $s_{1-\text{hc}} \neq s_{2-\text{hc}}$ ). This is confirmed by considering a honeycomb PC with  $s_{1-\text{hc}} = 191$  nm and  $s_{2-\text{hc}} = 320$  nm [right panel of Fig. 1(b)]. Note that we keep the same air-hole filling factor [i.e., a constant  $(s_{1-\text{hc}}^2 + s_{2-\text{hc}}^2)/2a^2$ ], which ensures the band structures of the PCs do not change much in frequency. As shown in Fig. 1(b), a photonic band gap occurs between the first and second TE bulk bands (shaded in yellow). By keeping the same air-hole filling factor and further increasing the amplitude of broken inversion symmetry, we have a honeycomb PC with  $s_{1-\text{hc}} = 0$  nm and  $s_{2-\text{hc}} = 373$  nm [right panel of Fig. 1(c)]. A larger band gap is found between  $0.263c/a$  and  $0.318c/a$ , where  $c$  is the speed of light in vacuum [shaded in yellow in Fig. 1(c)].

With regard to the TM polarization, we start with a hole-type triangular PC [cyan hexagon in Fig. 1(d)], and the unit cell consists of a central hexagonal air hole that is characterized by two side lengths, i.e.,  $s_{1-\text{tr}}$  and  $s_{2-\text{tr}}$ . Note that this unit cell can also be effectively viewed as the unit cell of a rod-type honeycomb PC, whose unit cell consists of two hexagonal-profile dielectric rods at the corners. For this kind of PC, the frequency degeneracy of the TM Dirac cone can be achieved at the PC with  $s_{1-\text{tr}} = s_{2-\text{tr}} = 153$  nm [air-hole filling factor of 0.36, which is the same as that of the PC in Fig. 1(a)], as shown in Fig. 1(d). With the broken inversion symmetry ( $s_{1-\text{tr}} = 86$  nm and  $s_{2-\text{tr}} = 230$  nm), a tiny band gap is obtained between the first and second TM bands [shaded in yellow in Fig. 1(e)]. To further increase the size of the band gap, we also keep the same air-hole filling factor and consider a triangular-lattice PC with  $s_{1-\text{tr}} = 0$  nm and  $s_{2-\text{tr}} = 373$  nm [left panel of Fig. 1(f)]. Shaded in yellow, there is a band gap ranging from  $0.281c/a$  to  $0.292c/a$  for TM polarization, which is covered by the frequency range of the TE band gap in Fig. 1(c). Interestingly, unit cells in Figs. 1(c) and 1(f) can be obtained by two different choices of the unit cell in the same bulk crystal (labeled as VPC1),

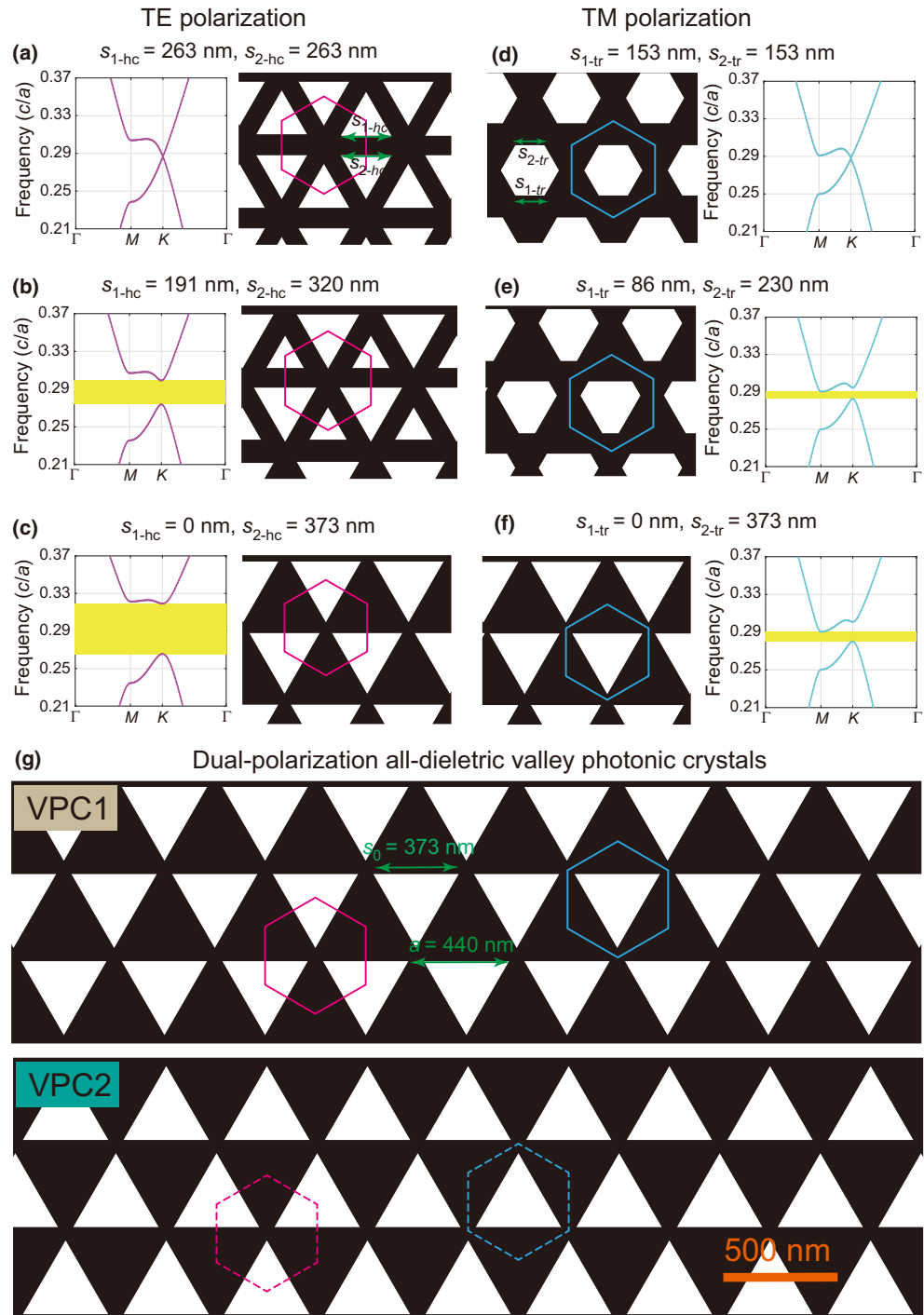


FIG. 1. Dual-polarization all-dielectric valley photonic crystals (VPCs). The designed PC consists of periodic air holes (white) in the dielectric background (black). (a)–(c) The evolution of two lowest TE band dispersions and the corresponding unit cells of honeycomb-lattice PC (pink hexagon). The unit cell of honeycomb-lattice PC consists of two triangular air holes at the corner, i.e., one with the side length of  $s_{1-hc}$  and the other with  $s_{2-hc}$ . (d)–(f) The evolution of two lowest TM band dispersions and the corresponding unit cells of triangle-lattice PC (cyan hexagon). The unit cell of triangle-lattice PC consists of a hexagonal air hole whose side lengths are labeled  $s_{1-tr}$  and  $s_{2-tr}$ . Note that TE and TM Dirac cones are achieved at the PCs with  $s_{1-hc}=s_{2-hc}$  and  $s_{1-tr}=s_{2-tr}$ . With the inversion symmetry breaking ( $s_{1-hc}\neq s_{2-hc}$  or  $s_{1-tr}\neq s_{2-tr}$ ), TE or TM band gap occurs (shaded in yellow). (g) Schematic of the dual-polarization VPC with the lattice constant  $a=440 \text{ nm}$  and the side length of air hole  $s_0=373 \text{ nm}$ . In this work, the dielectric background has a permittivity tensor  $\epsilon_r=\text{diag}(n_{\text{TE}}^2, n_{\text{TE}}^2, n_{\text{TM}}^2)$ . Here,  $n_{\text{TE}}=2.92$  and  $n_{\text{TM}}=2.51$  are the effective refractive indices of the dielectric background, based on the refractive indices of TE<sub>0</sub> and TM<sub>0</sub> mode indices of 320-nm-thick silicon slab around the wavelength of 1550 nm, respectively. A scale bar of 500 nm is included.

as shown in the top panel of Fig. 1(g). This means that the VPC1 has a common band gap for both TE and TM polarizations. In addition, the inversion-symmetric partner of VPC1 is also easy to realize by rotating it through an angle of  $180^\circ$ , which is shown in the bottom panel of Fig. 1(g) and labeled as VPC2.

### III. VALLEY-CONTRASTING PHYSICS AND DUAL-POLARIZATION VALLEY-DEPENDENT EDGE STATES

Although the bulk band structures of VPC2 are identical to those of VPC1, their topological properties are distinct and characterized by different valley Chern numbers. Based on topological physics [5,6,37], the valley-dependent topological index is defined as  $C_{K/K'} = \tau_z \text{sgn}(\Delta)/2$ . Here,  $\tau_z$  is the  $z$  component of Pauli matrix with  $\tau_z = +1$  for the  $K$  valley and  $\tau_z = -1$  for the  $K'$  valley, and  $2\Delta$  denotes the frequency difference between the frequencies of two valley bulk modes. The valley Chern number is given by  $C_V = C_K - C_{K'} = \text{sgn}(\Delta)$ . On the other hand, as a pair of pseudospins, modes at the two inequivalent  $K$  and  $K'$  valleys carry valley-dependent magnetic momentum  $m(K, K') = \tau_z \mu_B^*$ , where  $\mu_B^*$  is the effective Bohr magneton at the bottom band and  $\text{sgn}(\mu_B^*) = \text{sgn}(\Delta)$  [37]. In a PC, the effective “magnetic” momentum is related to the phase vortex of the electromagnetic fields, where  $\tau_z \text{sgn}(\mu_B^*) = +1$  or  $-1$  represents that the phase vortex increases clockwise (CW) or counterclockwise (CCW) by  $2\pi$ . Therefore, it is easy to determine the valley Chern number by exploring the phase vortex of bulk modes at different valleys. Figure 2(a) shows the  $H_z$  phase distributions for TE1 bulk modes at the two valleys. For VPC1, the CW (CCW) phase vortex at the  $K'$  ( $K$ ) valley indicates the topological valley index  $C_{K'} = +1/2$  ( $C_K = -1/2$ ) and thus we have the valley Chern number  $C_V = C_K - C_{K'} = -1$ . This also leads to the valley-chirality locking feature that the bulk mode at the  $K$  or  $K'$  valley can be selectively excited by using a chiral source with the same phase vortex. In contrast, the chirality of phase vortex, valley indices, and valley Chern number of VPC2 are opposite to those of VPC1. Similarly, the topological properties of the first TM bulk band can be retrieved from the  $E_z$  phase distributions, as shown in Fig. 2(b).

The topology of the TE or TM band gap  $C_V^{\text{gap}}$  depends on the summation of valley Chern numbers of the TE or TM bands  $C_V^n$  below the band gap, i.e.,  $C_V^{\text{gap}} = \sum_n C_V^n$ , where  $n$  is the TE or TM band index. In regard to our designed PC, the topology of TE or TM gap [shaded in yellow of Figs. 1(c) or 1(f)] only depends on the valley Chern number of the first TE or TM bulk band. Based on the analysis of valley-contrasting physics in the previous paragraph, the TE (TM) gap of VPC1 is characterized by the valley Chern number  $C_V^{\text{TEgap}} = -1$  ( $C_V^{\text{TMgap}} = -1$ ) and

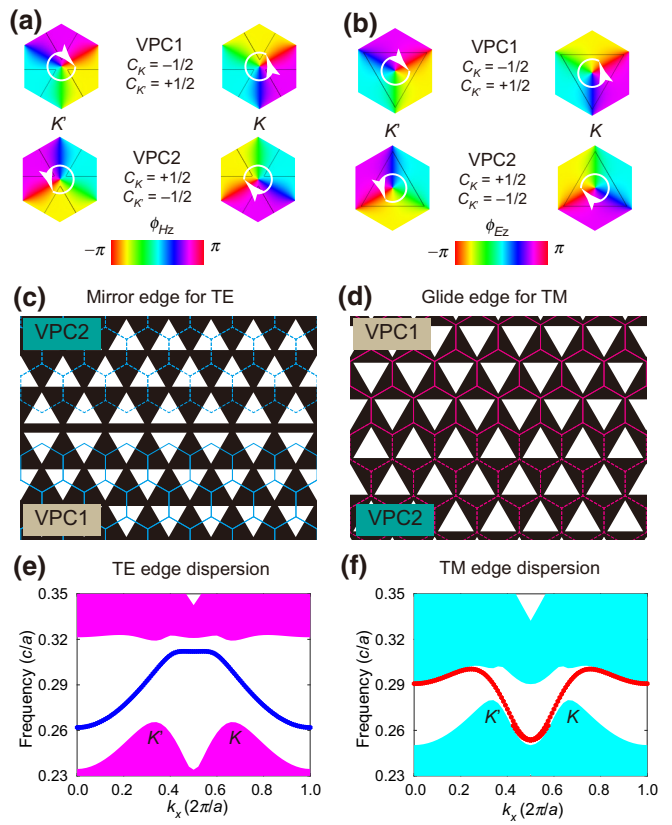


FIG. 2. Valley-contrasting physics and dual-polarization valley-dependent edge states. Phase distributions of (a)  $H_z$  and (b)  $E_z$  fields for TE and TM bulk modes at the  $K$  or  $K'$  valley, indicating the valley-chirality locking property. (c),(d) Schematics of edges with valley-dependent edge modes for TE and TM polarizations. Owing to the difference between the unit cells of the PC for the TE and TM polarizations, these two edges are of different shapes. For the TE polarization, by putting VPC2 (upper) above VPC1 (lower), the edge has the mirror-flip symmetry (abbreviated to “mirror edge”). For the TM polarization, by putting VPC1 (upper) above VPC2 (lower), the edge has glide-plane symmetry (abbreviated to “glide edge”). (e),(f) Band dispersions of edge modes for (e) TE polarization at mirror edge and (f) TM polarization at glide edge as a function of the wave vector along the  $x$  direction, i.e.,  $k_x$ . Valley-dependent edge modes are found at both edges. The group velocities have opposite directions because they are determined by the difference of valley Chern number across the domain wall.

that of VPC2 by  $C_V^{\text{TEgap}} = +1$  ( $C_V^{\text{TMgap}} = +1$ ). As the band gaps of VPC1 and VPC2 are topologically distinct, edge modes should be found at the interface of the domain wall between them. Note that these interfaces should be different shapes because of the different configurations of PC unit cells between TE and TM polarizations. For the TE polarization, by putting VPC2 (top, with dashed hexagon) above VPC1 (bottom, with solid hexagon), the edge has mirror-flip symmetry [Fig. 2(c), abbreviated to “mirror edge”]. For the TM polarization, by putting VPC1 (top,

with solid hexagon) above VPC2 (bottom, with dashed hexagon), the edge has glide-plane symmetry [Fig. 2(d)], abbreviated to “glide edge”]. Figures 2(e) and 2(f) show the dispersions of the corresponding edge modes (marked by red and blue lines). The pink and cyan regions are the projection bands of the TE and TM bulk modes, respectively. Note that the group velocity direction of the TE (TM) edge modes at the  $K'$  valley is positive (negative), and vice versa for the  $K$  valley. This is in agreement with the bulk-edge correspondence, for example, that the difference of the valley-dependent topological index at the  $K'$  valley crossing the domain wall (i.e.,  $C_{K'}^{\text{bottom}} - C_{K'}^{\text{top}}$ ) is +1 (−1) for the TE (TM) polarization. On the other hand, since the TE band gap has a different size to the TM case, the TM (TE) edge mode may be leaked in the bulk of the TE (TM) mode, which results in the decreasing of the optical bandwidth of VPC devices. We also notice that the designed VPC has a common band gap from 1507 to 1566 nm for both TE and TM polarizations. This common band gap region purely supports TE and TM edge modes and thus enables us to design polarizing devices.

#### IV. TOPOLOGICAL VALLEY TRANSPORT OF EDGE MODES

Under the intervalley suppression of valley-dependent edge modes, robust transport of TE and TM edge modes can be achieved. To demonstrate the robustness of valley-dependent edge modes (i.e., topological valley transport), we design two different waveguides with the flat interface (top) and with the Z-bend interface (bottom), as schematically shown in Figs. 3(a) and 3(d). For the TE (TM) polarization, the interfaces are constructed by the mirror (glide) edge. In other words, the interface that supports TE-polarized topological valley transport is different to that of TM polarization. The composition of VPC1 and VPC2 has a size of  $36a \times 24\sqrt{3}a$  (corresponding to  $15.84 \mu\text{m} \times 18.29 \mu\text{m}$  in practice). The bent length between two corners is  $12a$ . Two  $\sqrt{3}a$ -width strip waveguides are connected with the input and output facets of the VPC interface (shaded in black). To improve the coupling efficiency, the line-defect PC waveguides are introduced at the interfaces between the strip waveguides and the interface of the domain wall [more details are shown in the insets b3 and b4 of Fig. 4(b)]. To explore the transmitted properties, we use the finite-difference time-domain method to obtain the full-wave simulation results by using MIT Electromagnetic Equation Propagation [38]. Perfectly matched layers with  $2a$  thickness are imposed at the boundaries of simulated regions to absorb the outgoing waves. For the TE or TM polarization, a line source with an  $E_y$ - or  $E_z$ -polarized component is placed at the left-hand waveguide, and a line detector is placed at the right-hand waveguide to measure the output energy fluxes. The width of the line source and line detector are the same

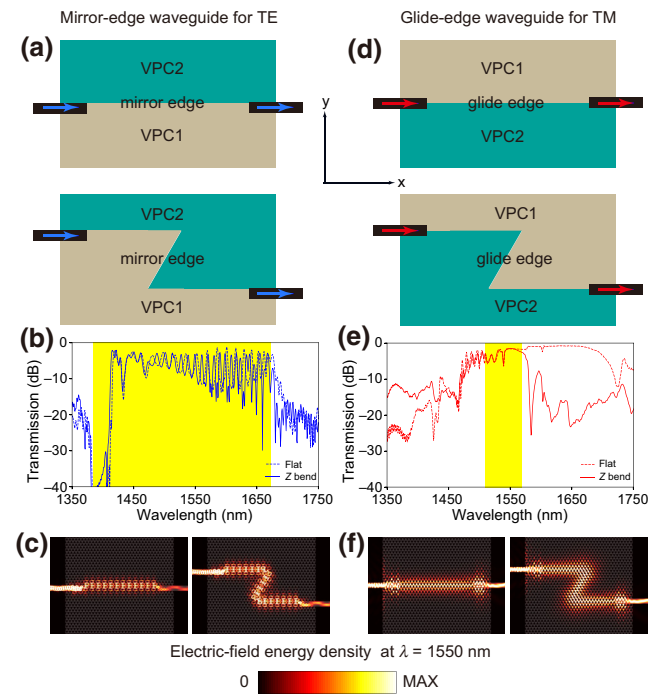


FIG. 3. Topological valley transport of TE and TM edge modes. (a),(d) Schematics of two waveguides with flat interface (top), and with Z-bend interface (bottom) based on (a) mirror edge and (d) glide edge. TE- or TM- polarized light is incident from the left and the transmission is measured at the right-hand output. (b),(e) The transmission spectra for two waveguides when (b) TE-polarized or (e) TM-polarized incident light is considered. Robust transport of edge modes can be achieved for both polarizations inside the band gap, proving the polarization independent topological valley transport. (c),(f) Electric-field energy density of transmitted electromagnetic waves at the wavelength of  $1550 \text{ nm}$  for (c) TE and (f) TM polarization.

as the width of the strip waveguides. The line source is a broadband Gaussian pulse with the central frequency  $f_c = 0.29c/a$  and the bandwidth  $df = 0.1c/a$ . The transmittance results are detected a certain time after the source is turned off.

Based on this simulated setup, the transmission spectra for two waveguides with a flat interface (dashed line) and with a Z-bend interface (solid line) are given in Figs. 3(b) and 3(e). The spectra are normalized by the transmittance of a  $\sqrt{3}a$ -width strip waveguide. We can see the same transmittance for the Z-shaped bend as the flat channel within the band gap, proving the broadband robustness of dual-polarization topological valley transport. This means the excited TE and TM edge modes inside the band gap are backscattering suppressed even when they meet sharp corners. For the transmission spectrum of the TE edge modes shown in Fig. 3(b), some of backscattered waves are induced when the excited TE edge modes encounter the right-hand output port. The interference between the forward and backward waves causes the peaks and dips

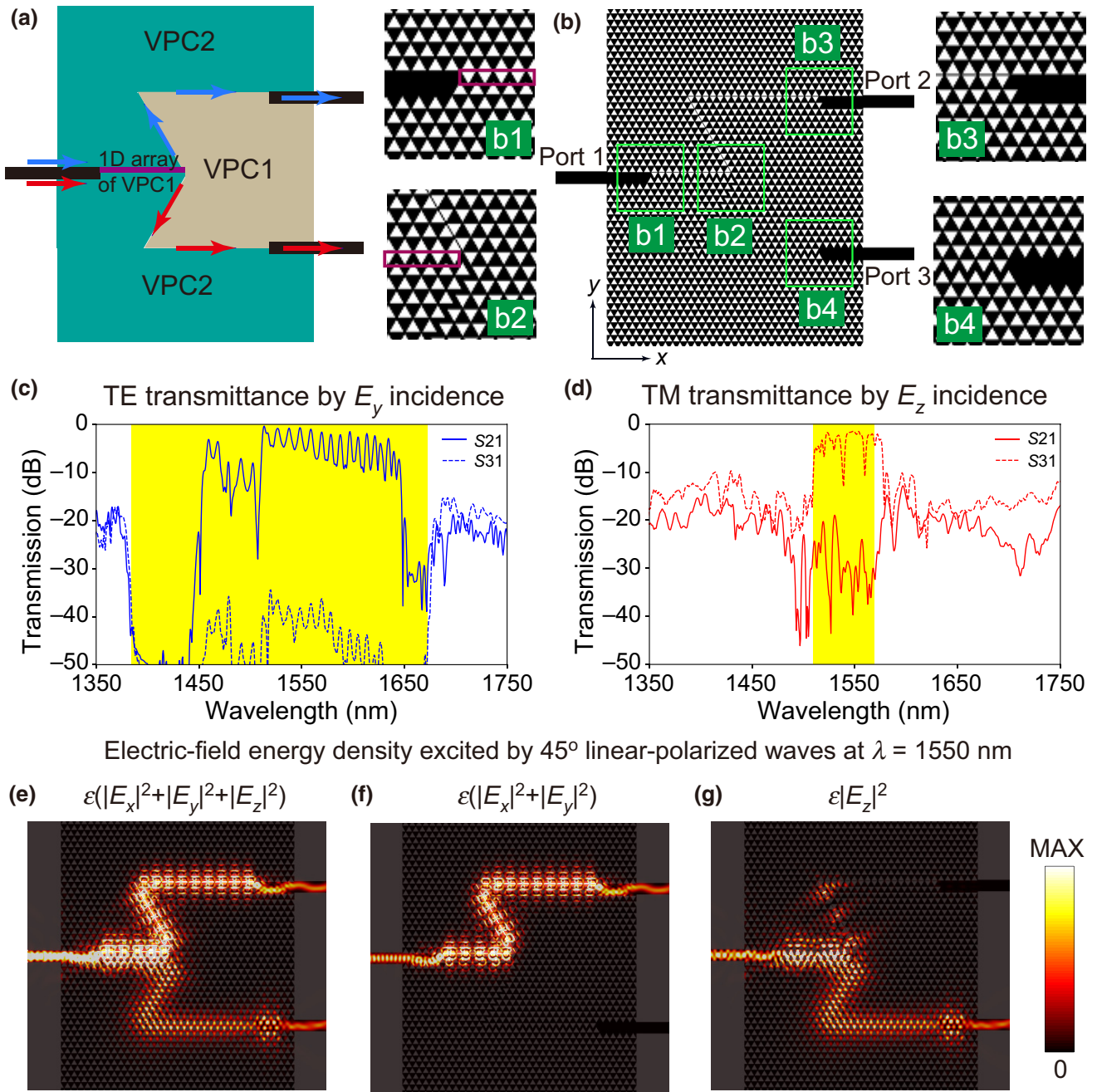


FIG. 4. Topological polarization beam splitter (PBS) based on dual-polarization VPCs. (a) Schematics and (b) details of topological PBS with the harpoon-shaped domain wall. The upward channel (output to port 2) is constructed by the mirror edge that supports TE edge modes, while the downward channel (output to port 3) is the glide edge that supports TM edge modes. Owing to the different configurations of PC unit cells of TE and TM polarizations, the interface between port 1 and the junction generates a line-defect region. To match with mirror and glide edge modes, we insert a 1D array of VPC1 inside the line-defect region (shaded in purple). (c),(d) The transmission spectra of TE and TM waves through the PBS. (c) TE-polarized or (d) TM-polarized light is incident from port 1 and the transmittances are measured at both port 2 ( $S_{21}$ , solid lines) and port 3 ( $S_{31}$ , dashed lines). (e)–(g) Distributions of electric-field energy density excited by  $45^\circ$  linear-polarized light at the wavelength of 1550 nm. (e) The 3D components of electric-field energy density confirm that both TE and TM edge modes are excited. Separately, (f) the TE-polarized waves (corresponding to the in-plane component of electric-field energy density) output to port 2, while (g) the TM-polarized waves (corresponding to that of out-of-plane component) output to port 3.

in the corresponding frequency region. This is due to the large band gap of TE modes that deviates from the effective Dirac Hamiltonian, and this is also confirmed in Fig. 2(e) in which the edge dispersion of TE modes cannot span the whole band gap. In contrast, the TM bulk band gap is much smaller [Fig. 1(f)] and thus the edge dispersion spans the whole band gap [Fig. 2(f)].

In particular, we also show the field patterns of the electric-field energy density of transmitted electromagnetic waves at the wavelength of 1550 nm in Figs. 3(c) and 3(f). The transmitted waves in the Z-bend interface are smoothly deflected by the 120° bends (60° sharp corners). The mode patterns are very similar to the results from the flat interface, proving the absence of reflection caused by the sharp corners. Note that the TE edge mode has a stronger field confinement than the TM edge mode, due to the larger band gap of TE polarization.

## V. A TOPOLOGICAL POLARIZATION BEAM SPLITTER BASED ON VALLEY PHOTONIC CRYSTALS

In the previous discussion, the edge modes and their robust transport are demonstrated independently for the TE and TM polarizations. In this section, we propose a PBS based on dual-polarization VPCs, by merging TE and TM edge modes in a single device. Figure 4(a) gives the schematic of topological PBS with a harpoon-shaped domain wall. More details of the structural design can be seen in Fig. 4(b). The footprint of the designed PBS is  $36a \times 24\sqrt{3}a$  (corresponding to  $15.84 \mu\text{m} \times 18.29 \mu\text{m}$  in practice). The upward channel (output to port 2) is constructed by the mirror edge that supports robust edge modes only for the TE polarization, while the downward channel (output to port 3) is the glide edge that supports robust edge modes only for the TM polarization. At all three ports, the line-defect PC waveguides are introduced to improve the coupling efficiency, as shown in the insets b1, b3, and b4 of Fig. 4(b). Owing to the different configurations of the unit cells of TE and TM polarizations, the interface between port 1 and the junction generates a line-defect region [shaded in purple of Fig. 4(a)]. To match with mirror and glide edge modes, the unit cell of VPC1 is arranged periodically along the  $x$  axis (i.e., 1D array of the unit cell of VPC1) in the line-defect region, highlighted as purple boxes in the insets b1 and b2 of Fig. 4(b). In the simulation, the setup of the input source and output detector are the same as in Fig. 3. A line source with an  $E_y$  (or  $E_z$ ) component is incident from port 1 and then excites TE- (or TM-) polarized propagating waves. At the right-hand ends, the transmittances are measured at port 2 ( $S_{21}$ , solid lines) and port 3 ( $S_{31}$ , dashed lines). For the TE-polarized transmittance in Fig. 4(c),  $S_{21}$  (blue solid line) has a high-transmission plateau ( $>-10 \text{ dB}$ ) from 1507 to 1646 nm, while  $S_{31}$  (blue dashed line) is

less than  $-35 \text{ dB}$  in this wavelength interval. In regard to the TM-polarized transmittance in Fig. 4(d),  $S_{31}$  (red dashed line) is obviously larger than  $S_{21}$  (red solid line) within the TM gap (from 1507 to 1566 nm). In other words, the transmission between  $S_{21}$  and  $S_{31}$  is distinct for both polarizations, indicating the separation functionality of TE and TM polarizations. The polarization extinction ratio (PER) between port 2 and port 3 is determined by the ratio between  $S_{21}$  and  $S_{31}$ , i.e.,  $\text{PER} = 10 \log_{10}(S_{21}/S_{31})$ . Within the whole dual-polarization band gap (from 1507 to 1566 nm), the simulated PER of such a device is greater than 10 dB.

To further intuitively observe the polarization beam-splitting effect, we also show the distributions of electric-field energy density in Figs. 4(e)–4(g) for different electric-field components when the PBS is excited by 45° linear-polarized light at the wavelength of 1550 nm. As the incident source can be orthogonally divided into  $E_y$ - and  $E_z$ -polarized components, both TE and TM edge modes are excited simultaneously. This is confirmed by the distribution of electric-field energy density shown in Fig. 4(e). Although high electric-field energy density can be found at both the upper and lower channels, they correspond to electromagnetic waves with different polarizations. Separately, the TE-polarized waves [corresponding to the in-plane component of electric-field energy density in Fig. 4(f)] propagates along the upward channel and outputs to port 2, while the TM-polarized waves [corresponding to the out-of-plane component of electric-field energy density in Fig. 4(g)] propagates along the downward channel and outputs to port 3. In Fig. 4(g), there is some scattering happening on the top side of the PBS, induced by the coupling of TM-polarized waves along the mirror edge [see region b3 of Fig. 4(b)]. Based on the analysis of edge states (see Fig. 2), the mirror edge (corresponding to the top side of the PBS waveguide in Fig. 4) supports TE-polarized topological edge states. However, the mirror edge also supports TM-polarized edge states inside the bandgap. When TM waves propagate to the junction of the PBS [the inset b2 in Fig. 4(b)], a part of them is coupled to the top side of the waveguide. Note that the TM waves propagating along the top side are not under the topological protection, so these coupling waves encounter scattering at the sharp-bending corner of the top side, as shown in Fig. 4(g).

In a word, the proposal of a harpoon-shaped topological PBS provides an alternative method for the design of on-chip polarizing devices, significantly different from conventional methods such as modal evolution [39,40]. The sharp-bending interfaces facilitate the reduction of PBS device size. The two output channels based on two different kinds of valley-dependent interfaces separate TE- and TM-polarized waves naturally, so the tolerance of fabrication bias of PBS can be released while maintaining good functionality of polarization separation.

## VI. CONCLUSIONS

In summary, we realize dual-polarization all-dielectric VPCs. For both TE and TM polarizations, valley-dependent edge modes are achieved. We perform numerical simulations to demonstrate dual-polarization topological valley transport along sharp-bend interfaces. In addition, a harpoon-shaped PBS based on the dual-polarization feature of VPCs is proposed and the simulated transmittances of this PBS confirm the good separation functionality of TE- and TM-polarized waves within the whole dual-polarization band gap. In this way, one can load two different optical signals into TE- and TM-polarized waves separately, so that the optical information-processing capacity of dual-polarization VPCs can be double that of single polarization. The introduction of polarization DOF into valley photonic systems gives more opportunity for the flexible control of light. Furthermore, it has potential applications in the design of topologically protected polarization multiplexing nanophotonic devices for modern information-processing systems, in particular for silicon photonics and integrated quantum optics.

## ACKNOWLEDGMENTS

This work was supported by National Key Research and Development Program of China (Grant No. 2019YFB2203502), National Natural Science Foundation of China (Grants No. 62035016, No. 12074443, and No. 11904421), Guangdong Basic and Applied Basic Research Foundation (Grant No. 2019B151502036), Guangzhou Science, Technology and Innovation Commission (Grants No. 202002030322 and No. 202102020693), Fundamental Research Funds for the Central Universities (Grant No. 2021qntd27).

- [1] L. Lu, J. D. Joannopoulos, and M. Soljacic, Topological photonics, *Nat. Photonics* **8**, 821 (2014).
- [2] T. Ozawa, H. M. Price, A. Amo, N. Goldman, M. Hafezi, L. Lu, M. C. Rechtsman, D. Schuster, J. Simon, O. Zilberberg, and I. Carusotto, Topological photonics, *Rev. Mod. Phys.* **91**, 015006 (2019).
- [3] F. Haldane and S. Raghu, Possible Realization of Directional Optical Waveguides in Photonic Crystals with Broken Time-Reversal Symmetry, *Phys. Rev. Lett.* **100**, 013904 (2008).
- [4] L.-H. Wu and X. Hu, Scheme for Achieving a Topological Photonic Crystal by Using Dielectric Material, *Phys. Rev. Lett.* **114**, 223901 (2015).
- [5] T. Ma and G. Shvets, All-Si valley-Hall photonic topological insulator, *New J. Phys.* **18**, 025012 (2016).
- [6] X.-D. Chen, F.-L. Zhao, M. Chen, and J.-W. Dong, Valley-contrasting physics in all-dielectric photonic crystals: Orbital angular momentum and topological propagation, *Phys. Rev. B* **96**, 020202(R) (2017).

- [7] S. Barik, A. Karasahin, C. Flower, T. Cai, H. Miyake, W. DeGottardi, M. Hafezi, and E. Waks, A topological quantum optics interface, *Science* **359**, 666 (2018).
- [8] M. I. Shalaev, W. Walasik, A. Tsukernik, Y. Xu, and N. M. Litchinitser, Robust topologically protected transport in photonic crystals at telecommunication wavelengths, *Nat. Nanotechnol.* **14**, 31 (2019).
- [9] X.-T. He, E.-T. Liang, J.-J. Yuan, H.-Y. Qiu, X.-D. Chen, F.-L. Zhao, and J.-W. Dong, A silicon-on-insulator slab for topological valley transport, *Nat. Commun.* **10**, 872 (2019).
- [10] X.-D. Chen, W.-M. Deng, F.-L. Shi, F.-L. Zhao, M. Chen, and J.-W. Dong, Direct Observation of Corner States in Second-Order Topological Photonic Crystal Slabs, *Phys. Rev. Lett.* **122**, 233902 (2019).
- [11] B.-Y. Xie, G.-X. Su, H.-F. Wang, H. Su, X.-P. Shen, P. Zhan, M.-H. Lu, Z.-L. Wang, and Y.-F. Chen, Visualization of Higher-Order Topological Insulating Phases in Two-Dimensional Dielectric Photonic Crystals, *Phys. Rev. Lett.* **122**, 233903 (2019).
- [12] Y. Ota, F. Liu, R. Katsumi, K. Watanabe, K. Wakabayashi, Y. Arakawa, and S. Iwamoto, Photonic crystal nanocavity based on a topological corner state, *Optica* **6**, 786 (2019).
- [13] M. Jung, R. Gladstone, and G. Shvets, Nanopolaritonic second-order topological insulator based on graphene plasmons, *Adv. Photonics* **2**, 046003 (2020).
- [14] M. Hafezi, S. Mittal, J. Fan, A. Migdall, and J. M. Taylor, Imaging topological edge states in silicon photonics, *Nat. Photonics* **7**, 1001 (2013).
- [15] M. A. Bandres, S. Wittek, G. Harari, M. Parto, J. Ren, M. Segev, D. N. Christodoulides, and M. Khajavikhan, Topological insulator laser: Experiments, *Science* **359**, eaar4005 (2018).
- [16] S. Mittal, V. V. Orre, G. Zhu, M. A. Gorlach, A. Poddubny, and M. Hafezi, Photonic quadrupole topological phases, *Nat. Photonics* **13**, 692 (2019).
- [17] A. Blanco-Redondo, B. Bell, D. Oren, B. J. Eggleton, and M. Segev, Topological protection of biphoton states, *Science* **362**, 568 (2018).
- [18] J. Noh, W. A. Benalcazar, S. Huang, M. J. Collins, K. P. Chen, T. L. Hughes, and M. C. Rechtsman, Topological protection of photonic mid-gap defect modes, *Nat. Photonics* **12**, 408 (2018).
- [19] H. Zhong, S. Xia, Y. Zhang, Y. Li, D. Song, C. Liu, and Z. Chen, Nonlinear topological valley Hall edge states arising from type-II Dirac cones, *Adv. Photonics* **3**, 056001 (2021).
- [20] J.-W. Dong, X.-D. Chen, H. Zhu, Y. Wang, and X. Zhang, Valley photonic crystals for control of spin and topology, *Nat. Mater.* **16**, 298 (2017).
- [21] F. Gao, H. Xue, Z. Yang, K. Lai, Y. Yu, X. Lin, Y. Chong, G. Shvets, and B. Zhang, Topologically protected refraction of robust kink states in valley photonic crystals, *Nat. Phys.* **14**, 140 (2018).
- [22] J. Ma, X. Xi, and X. Sun, Topological photonic integrated circuits based on valley kink states, *Laser Photonics Rev.* **13**, 1900087 (2019).
- [23] D. Smirnova, A. Tripathi, S. Kruk, M. S. Hwang, H. R. Kim, H. G. Park, and Y. Kivshar, Room-temperature lasing from nanophotonic topological cavities, *Light: Sci. Appl.* **9**, 127 (2020).

- [24] Y. Zeng, U. Chattopadhyay, B. Zhu, B. Qiang, J. Li, Y. Jin, L. Li, A. G. Davies, E. H. Linfield, B. Zhang, Y. Chong, and Q. J. Wang, Electrically pumped topological laser with valley edge modes, *Nature* **578**, 246 (2020).
- [25] Y. Chen, X.-T. He, Y.-J. Cheng, H.-Y. Qiu, L.-T. Feng, M. Zhang, D.-X. Dai, G.-C. Guo, J.-W. Dong, and X.-F. Ren, Topologically Protected Valley-Dependent Quantum Photonic Circuits, *Phys. Rev. Lett.* **126**, 230503 (2021).
- [26] J. D. Joannopoulos, S. G. Johnson, J. N. Winn, and R. D. Meade, *Photonic crystals: Molding the flow of light* (Princeton university press, Princeton, New Jersey, 2011).
- [27] L. He, H. Zhang, W. Zhang, Y. Wang, and X. Zhang, Topologically protected vector edge states and polarization beam splitter by all-dielectric valley photonic crystal slabs, *New J. Phys.* **23**, 093026 (2021).
- [28] X.-T. He, J.-W. Liu, F.-L. Shi, K. Shen, W.-J. Chen, X.-D. Chen, and J.-W. Dong, Dual-polarization two-dimensional valley photonic crystals, *Sci. China: Phys., Mech. Astron.* **65**, 284212 (2022).
- [29] L. Tao, A. R. Zakharian, M. Fallahi, J. V. Moloney, and M. Mansuripur, Design of a compact photonic-crystal-based polarizing beam splitter, *IEEE Photonics Technol. Lett.* **17**, 1435 (2005).
- [30] B. Shen, P. Wang, R. Polson, and R. Menon, An integrated-nanophotonics polarization beamsplitter with  $2.4 \times 2.4 \mu\text{m}^2$  footprint, *Nat. Photonics* **9**, 378 (2015).
- [31] Y. Zhang, Y. He, J. Wu, X. Jiang, R. Liu, C. Qiu, X. Jiang, J. Yang, C. Tremblay, and Y. Su, High-extinction-ratio silicon polarization beam splitter with tolerance to waveguide width and coupling length variations, *Opt. Express* **24**, 6586 (2016).
- [32] C. Li, M. Zhang, H. Xu, Y. Tan, Y. Shi, and D. Dai, Subwavelength silicon photonics for on-chip mode-manipulation, *PhotonIX* **2**, 11 (2021).
- [33] M. J. Collins, F. Zhang, R. Bojko, L. Chrostowski, and M. C. Rechtsman, Integrated optical dirac physics via inversion symmetry breaking, *Phys. Rev. A* **94**, 063827 (2016).
- [34] X.-D. Chen, F.-L. Shi, H. Liu, J.-C. Lu, W.-M. Deng, J.-Y. Dai, Q. Cheng, and J.-W. Dong, Tunable Electromagnetic Flow Control in Valley Photonic Crystal Waveguides, *Phys. Rev. Appl.* **10**, 044002 (2018).
- [35] S.-I. Takayama, H. Kitagawa, Y. Tanaka, T. Asano, and S. Noda, Experimental demonstration of complete photonic band gap in two-dimensional photonic crystal slabs, *Appl. Phys. Lett.* **87**, 061107 (2005).
- [36] S. G. Johnson and J. D. Joannopoulos, Block-iterative frequency-domain methods for Maxwell's equations in a planewave basis, *Opt. Express* **8**, 173 (2001).
- [37] D. Xiao, W. Yao, and Q. Niu, Valley-Contrasting Physics in Graphene: Magnetic Moment and Topological Transport, *Phys. Rev. Lett.* **99**, 236809 (2007).
- [38] A. Oskooi, D. Roundy, M. Ibanescu, P. Bermel, J. D. Joannopoulos, and S. G. Johnson, Meep: A flexible free-software package for electromagnetic simulations by the FDTD method, *Comput. Phys. Commun.* **181**, 687 (2010).
- [39] M. R. Watts, H. A. Haus, and E. P. Ippen, Integrated mode-evolution-based polarization splitter, *Opt. Lett.* **30**, 967 (2005).
- [40] W. Yuan, K. Kojima, B. Wang, T. Koike-Akino, K. Parsons, S. Nishikawa, and E. Yagyu, Mode-evolution-based polarization rotator-splitter design via simple fabrication process, *Opt. Express* **20**, 10163 (2012).